Numerical Simulations of the Apollo S-IVB Artificial Impacts on the Moon

A. Rajšić, K. Miljković, N. Wójcicka, G. Collins, K. Onodera, T. Kawamura, P. Lognonné, Mark Wieczorek, I. Daubar

Earth and Space Science

RESEARCH ARTICLE
10.1029/2021EA001887

Numerical Simulations of the Apollo S-IVB Artificial Impacts on the Moon

A. Rajšić[1], K. Miljković[1], N. Wójcicka[2], G. S. Collins[2], K. Onodera[3,4,5], T. Kawamura[3], P. Lognonné[3], M. A. Wieczorek[6], and I. J. Daubar[7]

[1]School of Earth and Planetary Sciences, Space Science and Technology Center, Curtin University, Perth, WA, Australia, [2]Imperial College London, London, UK, [3]Institute de Physique du Globe de Paris, Paris, France, [4]Department of Space and Astronautical Science, School of Physical Sciences, The Graduate University for Advanced Studies, SOKENDAI, Sagamihara, Japan, [5]Institute of Space and Astronautical Science, Japan Aerospace Exploration Agency, Sagamihara, Japan, [6]Observatoire de la Côte d'Azur, CNRS, Laboratoire Lagrange, Université Côte d'Azur, Nice, France, [7]Department of Earth, Environmental and Planetary Sciences, Brown University, Providence, RI, USA

Abstract The third stage of the Saturn IV rocket used in the five Apollo missions made craters on the Moon ~30 m in diameter. Their initial impact conditions were known, so they can be considered controlled impacts. Here, we used the iSALE-2D shock physics code to numerically simulate the formation of these craters, and to calculate the vertical component of seismic moment (~4×10^{10} Nm) and seismic efficiency (~10^{-6}) associated with these impacts. The irregular booster shape likely caused the irregular crater morphology observed. To investigate this, we modeled six projectile geometries, with footprint area between 3 and 105 m^2, keeping the mass and velocity of the impactor constant. We showed that the crater depth and diameter decreased as the footprint area increased. The central mound observed in lunar impact sites could be a result of layering of the target and/or low density of the projectile. Understanding seismic signatures from impact events is important for planetary seismology. Calculating seismic parameters and validating them against controlled experiments in a planetary setting will help us understand the seismic data received, not only from the Moon, but also from the InSight Mission on Mars and future seismic missions.

Plain Language Summary Observations of meteoroid strikes on the Moon, including artificial impacts made by the Saturn boosters from the Apollo missions, present valuable information for connecting impact conditions with seismic properties of the lunar and planetary crusts. These artificial impacts on the Moon were made by irregularly shaped spacecraft with low density. We numerically simulated these artificial impacts, using several different projectile geometries in order to represent the spacecraft's low density and shape. We found that the projectile representation affected the crater size. We calculated the amount of energy transferred into seismic waves and seismic moment created in these impacts to be consistent with previous studies. These parameters did not change with different projectile representations, but were affected by the material properties of the impact site. The aim is to use the results from the controlled lunar impacts to help understand the seismic signatures of impacts on Mars.

Key Points:

- Numerical impact simulations of the Apollo rocket stage drop on the Moon
- Projectile geometry affects cratering process, cratering efficiency, and momentum transfer
- Estimates of the seismic moment and seismic efficiency in these impacts

Supporting Information:

Supporting Information may be found in the online version of this article.

Correspondence to:

A. Rajšić,
andrea.rajsic@postgrad.curtin.edu.au

Citation:

Rajšić, A., Miljković, K., Wójcicka, N., Collins, G. S., Onodera, K., Kawamura, T., et al. (2021). Numerical simulations of the Apollo S-IVB artificial impacts on the Moon. *Earth and Space Science*, *8*, e2021EA001887. https://doi.org/10.1029/2021EA001887

Received 13 JUN 2021
Accepted 3 NOV 2021

Author Contributions:

Conceptualization: A. Rajšić, P. Lognonné, M. A. Wieczorek
Data curation: A. Rajšić
Formal analysis: A. Rajšić
Investigation: A. Rajšić
Methodology: A. Rajšić
Supervision: K. Miljković
Validation: A. Rajšić, N. Wójcicka, G. S. Collins
Visualization: A. Rajšić
Writing – original draft: A. Rajšić
Writing – review & editing: A. Rajšić, K. Miljković, G. S. Collins, K. Onodera, T. Kawamura, I. J. Daubar

1. Introduction

The NASA InSight Mission has been recording seismic activity on the surface of Mars since late 2018 (e.g., Banerdt et al., 2020). However, to date none of these signals have been unambiguously associated with an impact event (Daubar et al., 2020). This calls for further investigation of meteorite strikes and the relationship between impact parameters and the amplitude of the seismic signals they generate. The artificial craters that were made by the Saturn IV boosters (S-IVB) impacting the Moon (Wagner et al., 2017) represent large scale impact experiments (Figure 1). They provide a valuable link between known impact conditions and resulting crater size. Moreover, the seismic signals generated by these impacts were recorded by the Apollo seismic network operating on the Moon at the time, which provided information about impact-induced seismicity on the Moon (e.g., Gudkova et al., 2015; Latham et al., 1970; Lognonné, 2005; Lognonné & Mosser, 1993; Lognonné et al., 2009; Onodera et al., 2021; Toksöz et al., 1974).

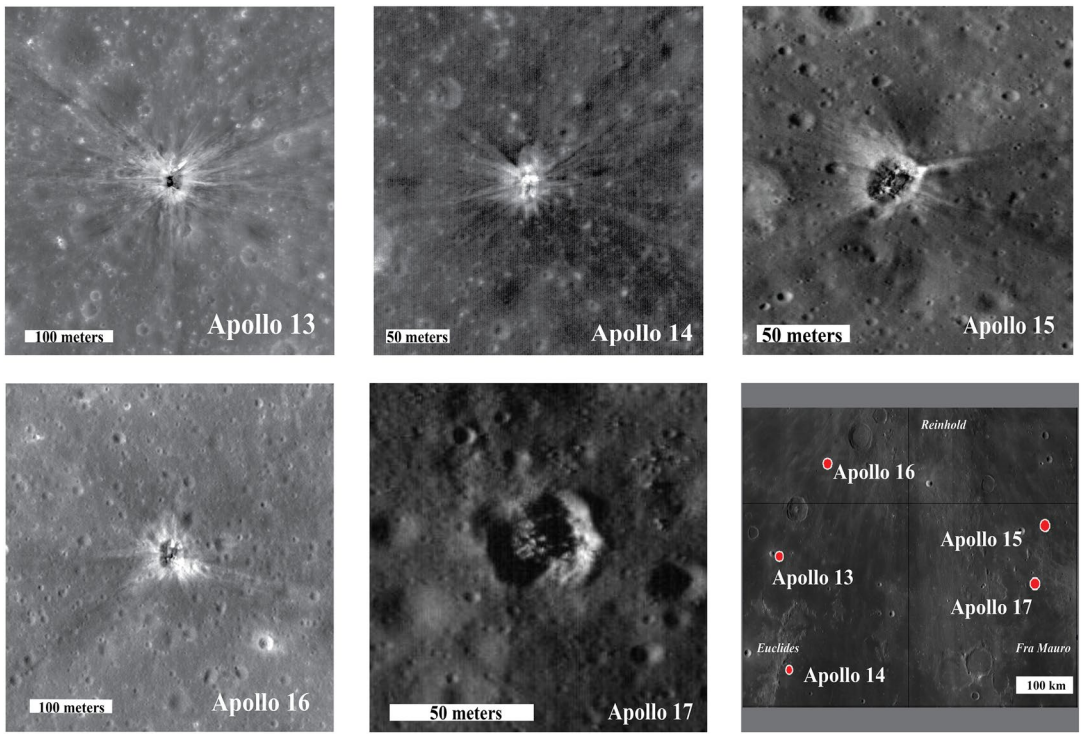

Figure 1. Apollo artificial craters on the Moon. Craters are all asymmetric and they show central mounds at the bottom. Ejecta around craters do not include resolved rocks, under resolution of 0.5 m/px. (LROC NAC images: Apollo 13, M109420042LE; Apollo 14, M1162633177R; Apollo 15, M160030722L; Apollo 16, M183689432L; and Apollo 17, M131731837R. The scale is 50 or 100 m.)

Several Apollo S-IVB boosters impacted into regolith overlying mare basalt geological units on the lunar near side hemisphere during the period of seismic monitoring by Apollo. All Apollo S-IVB booster impacts made elliptical craters (short axis in between 29 and 31.9 m and long axis in between 33.3 and 38.7 m). Plescia et al. (2016) used shadow method to estimate crater depth as 2–3 m from rim to the floor. However, this method takes into account that the bottom of the crater is the lowest point of the crater cavity, and these craters all have central mounds at the bottom (Figure 1). Furthermore, they argue that crater of 32.9 m in diameter should correspond to 6 m depth, which makes these craters shallower than natural impacts of same size. In this paper, we use depths inferred from shadow measurements as a lower bound, and those derived from crater scaling estimates for bowl-shaped craters as an upper bound, for comparison with our models.

The mass of the Saturn S-IVB combined with J2 engine and instrument ring was about 14 t. The booster was 17.8 m long and 6.6 m in diameter. It was made of aluminum and had a low bulk density of 23 $kg{\cdot}m^{-3}$ (e.g., Mc Fadden & Salzberg, 1970; Plescia et al., 2016; Wagner et al., 2017). In this work, we modeled an empty booster, without fuel (Mc Fadden & Salzberg, 1970). The impact speed at ground level was 2.543–2.66 $km{\cdot}s^{-1}$. The angle at which the booster trajectory intersected the surface was reported to be between 13.2 and 35° from vertical (e.g., Plescia et al., 2016), implying an almost vertical impact. On the other hand, given that the center of mass was located near the bottom of the booster, the booster likely tumbled during the fall causing the exact orientation of the booster at the point of impact to be unknown. Since the inspection of LROC images of the craters (Figure 1) did not reveal any boulders around the craters that might suggest that central mounds in these craters are the result of excavation into a rocky/stronger layer beneath the regolith, it has been proposed that the central mounds are residual impactor material (Plescia et al., 2016). To test this hypothesis, we simulated S-IVB booster impacts into a target consisting of a single layer of regolith. However, as the regolith thickness at the impact site is estimated to be 4–5 m (e.g., McKay et al., 1991), comparable to the estimated depth of the S-IVB transient craters, it is also possible that the central mound at the bottom of the crater is a consequence of the presence of stronger/rocky material beneath the regolith (Prieur et al., 2018).

Table 1
Numerical Representation of the Impactor: Description of Shape, CPPR in Vertical (CPPRV) and Horizontal Direction (CPPRH; Where CPPR Stands for "Cells Per Projectile Radius" and Defines the Resolution of the Whole Simulation) and Grid Spacing, Which Is the Physical Size of Each Cell

Case	Description	CPPRV	CPPRH	Grid spacing	Footprint area (m^2)
1	Right cylinder, $r = 5.8$ m	5	118	0.0496	105.6
2	Right cylinder, $r = 2.8$ m	22	56	0.0496	24.6
3	Thin shell, $r = 2.8$ m	16 (12)	89 (85)	0.03	24.6
4	Right cylinder, $r = 0.992$ m	169	20	0.0496	3
5	Sphere, $r = 1.06$ m	18 (10)	18 (10)	0.059 (0.1)	3
6	Sphere, $r = 2.3$ m	18 (10)	18 (10)	0.127 (0.2)	16.6
7	Sphere, $r = 2.3$ m	18 (10)	18 (10)	0.127 (0.2)	16.6

Note. In this work, there are two sets of simulations: crater formation simulations and pressure wave propagation from impact point into far field (CPPR parameters shown in bracket). The Cases 1–4 had the same resolution in both sets of simulations, while Cases 5–7 had higher resolution in crater formation runs than in pressure wave propagation. Cases 6 and 7 have the same impactor properties, but the target properties are different.

In this work, we explored the effects of the projectile shape on crater morphology, using the same target properties. In addition, for one projectile geometry we also considered a layered target scenario to investigate potential causes of central mound formation. We investigated the pressure wave propagation from the impact point, the seismic moment, and seismic efficiency associated with these impacts (e.g., Gudkova et al., 2015; Latham et al., 1970; McGarr et al., 1969). Previous work using seismic data from the Apollo artificial impacts (Latham et al., 1970) obtained a range of seismic efficiency of impacts near the Apollo 12 landing site to be between 1.8×10^{-6} and 10^{-5}. Here, we present comparable results, but we calculate the seismic efficiency from numerical impact simulations instead of the seismic data. Reproducing such impact events using numerical modeling contributes to our understanding of the seismicity induced by impact cratering events as well as the detectability of impacts in seismic data. Due to the lack of unambiguous impact events so far detected on Mars, this study is important for the InSight Mission science (Daubar et al., 2020).

2. Methods

We numerically simulated impact craters made by the Apollo S-IVB impacts on the Moon and quantified the seismic efficiency and seismic moment using the iSALE-2D shock physics code (Amsden et al., 1980; Collins et al., 2004; Wünnemann et al., 2006).

As the orientation of the S-IVB boosters at impact is not known, we explored the sensitivity of impact outcomes to booster (impactor) geometry by considering six idealized scenarios. The enforced axial symmetry of our impact geometry limited the scenarios that could be considered for vertical impact of right cylinders and spheroids. It is expected that penetration modes produced by more disk-like projectiles will be different from those caused by spherical projectiles (Walker, 1999). In order to explore the sensitivity of crater radius to projectile footprint area, which might give some insight into the possible range of crater ellipticity, our scenarios vary in radius and length depending on the projectile geometry presented. By footprint it is assumed as the surface area of the projectile as it impacts the surface. Mesh resolution limits combined with the need for a large domain to track the impact-generated waves implied that modeling the impactor as a thin-shelled, hollow container was computationally challenging. For this reason, we considered only one hollow-container geometry and for the other scenarios modeled, we adopted a more expedient approach where the impactor was modeled as a homogeneous porous or solid object. All projectiles had the same impactor mass (approximately 14 t) and speed (2.54 kms^{-1}) as reported in Plescia et al. (2016). The vertical impact velocity used in the simulations was not reduced to account for impact angle owing to the steep geometry of the impacts. The six simplified geometries considered were (Table 1, Figure 2):

1. A right cylinder of radius 5.8 m and height 0.5 m, made of 90% porous aluminum.
2. A right cylinder of radius 2.8 m and height 2.2 m, made of 90% porous aluminum.
3. A hollow right cylinder of radius 2.8 m and height 0.96 m, made of non-porous aluminum of interior thickness 0.12 m.

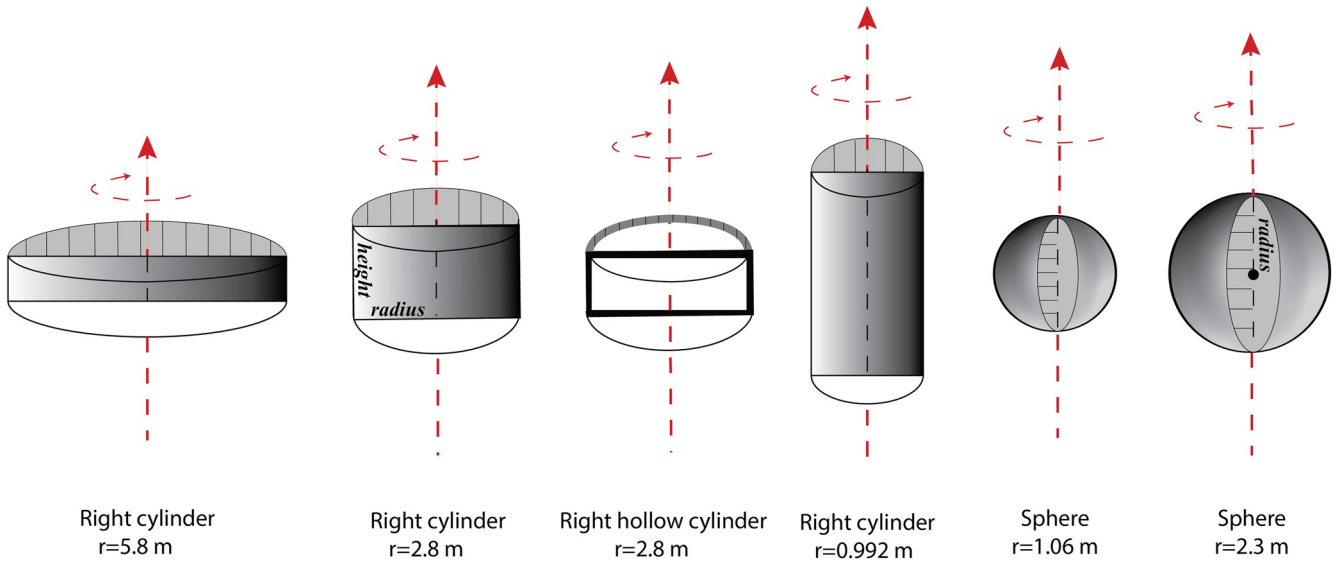

Figure 2. Different shapes of projectiles represented in this work (from left to right: Cases 1–6). The red axis is the symmetry axis in iSALE's cylindrical projection, meaning what we represent as rectangle or circle, is computed in the code as a cylinder and sphere. All impacts in this work happened parallel to the surface, hence perpendicular to the symmetry axis. Case 6, sphere with $r = 2.3$ m, was tested in both regolith and layered target.

4. A right cylinder of radius 0.992 m and height 16.7 m, made of 90% porous aluminum.
5. A sphere of radius 1.06 m, made of a non-porous aluminum.
6. A sphere of radius 2.3 m, made of 90% porous aluminum.

The contact area between the impactor and the target during impact contact and compression phase (hereby referred to as footprint) could have been between 34.2 m^2 (if the booster landed on the Moon along the short cylinder axis) and 117 m^2 (if the booster landed along the long axis). Our Cases 2 and 3 (24.6 m^2) are representative of the former and Case 1 (105.6 m^2) the latter. Cases 4 and 5 have much smaller footprint and are used as a sensitivity test to projectile geometry (Table 1).

The projectile material was described using the Tillotson equation of state (Tillotson, 1962) and the Johnson and Cook (JNCK) strength model for aluminum (Table S1 in Supporting Information S1 and Table 2) (Johnson & Cook, 1983; Liu et al., 2017). The simplified target was assumed to be uniform, made of 44% porous basalt. All targets were considered single layers made of regolith, except for Case 7 that comprised 5-m regolith overlaying fractured bedrock. Both Case 6 and Case 7 modeled the projectile as a 90% porous sphere and therefore provide a direct comparison between impact in a single-layer and double-layer target. This results in total seven different scenarios explored in this study. These target properties were used in previous simulations of small meteoroid impacts on similar targets on Mars (Rajšić et al., 2021; Wójcicka, Collins, Bastow, Teanby, et al., 2020).

The target material was described using revised Tillotson equation of state parameters for basalt, refined for use as a proxy for low-velocity impacts in basaltic regolith (Table S2 in Supporting Infrormation S1; Wójcicka, Collins, Bastow, Miljkovic, et al., 2020), and material (porosity and strength) parameters typical for lunar regolith (Colwell et al., 2007; McKay et al., 1991; Mitchell et al., 1974; Wilcox et al., 2005). The target's deviatoric strength was described using a simple pressure-dependent strength model (Lundborg, 1968) (Table 2). The porosity of the lunar regolith and fractured bedrock was included via $\epsilon - \alpha$ porosity model (e.g., Wünnemann et al., 2006). The bulk density of regolith was $\rho = 1{,}589$ kgm^{-3}, and the bulk sound speed 857 ms^{-1} ($C_b = \sqrt{B/\rho}$, where B is bulk modulus), and P-wave speed was 1,088 ms^{-1} ($C_p = \Delta s/\Delta t$, where Δs is distance and Δt is time, the method is described in detail further down). We used the ROCK strength model (Collins et al., 2004) to describe the shear strength of fractured bedrock. The material model for fractured bedrock was assumed to be similar to sandstone (Güldemeister & Wünnemann, 2017). Density of the fractured bedrock was $\rho = 2{,}150$ $kg{\cdot}m^{-3}$. Bulk speed of sound of the material (C_b) and P-wave speed (C_p) were

Table 2
Material Model Parameters for All Sets of Simulations (Liu et al., 2017; Rajšić et al., 2021; Wójcicka, Collins, Bastow, Teanby, et al., 2020)

Description	Symbol	Projectile	Bedrock	Regolith
Poisson ratio	ν	0.30	0.30	0.30
Strength at inf. pressure (intact; MPa)	Y_∞		170.	
Internal friction coeff. (intact)	μ_i		1.80	
Strength at zero pressure (damaged; KPa)	Y_{d0}			4.00
Friction coefficient (damaged)	μ_d		0.67	0.60
Strain coefficient	a	4.9×10^7		
Strain coefficient	b	1.57×10		
Strain coefficient	c	1.6×10^{-2}		
Strain exponent	n	1.67×10^{-1}		
Specific Heat Capacity (J/Kg/Kelvin)	C_p	896	1,000	1,000
Initial porosity	ϕ_0	0.90	0.25	0.44
Initial distension	α_0	10.00	1.33	1.80
Distension at onset of crushing	α_e	9.96	1.33	1.80
Distension at transition to power-law	α_x	1.00	1.10	1.15
Exponential compaction rate	κ	0.98	0.98	0.98
Ratio of porous/nonporous sound speed	χ	0.17	0.60	0.33
Volumetric strain at transition	ϵ_x	−2.35	−0.19	−0.46
Volumetric strain when fully compacted	ϵ_c	−2.35	−0.38	−0.72

1,558 ms^{-1} and 2,045 ms^{-1}, respectively (Rajšić et al., 2021). Material models for projectile and all targets are shown in Table 2.

Crater formation was simulated until after the transient crater was formed. The numerical mesh size was 400×400 cells, with variable projectile resolution, which was unavoidable due to irregular projectile shapes (Table 1). Referring to previous works, the transient crater was considered at the maximum excavation volume (Wünnemann et al., 2011). Figure 3 shows how transient crater diameter (D_{tc}) and transient crater depth (d_{tc}) were measured.

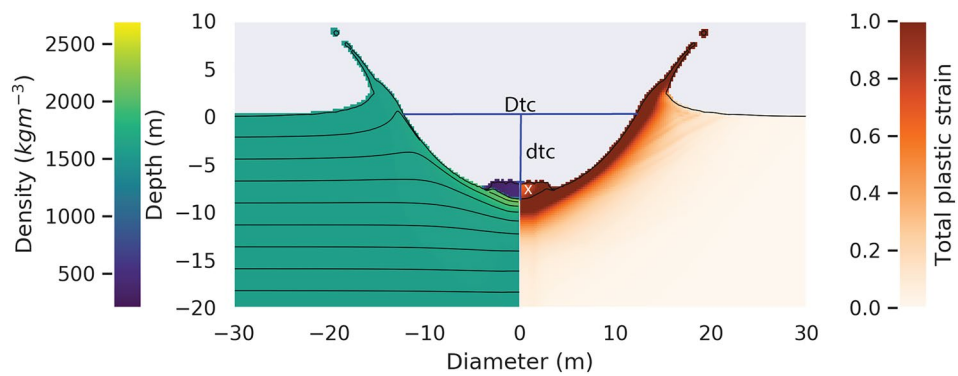

Figure 3. An example output from Case 5 showing a 2.3-m radius porous sphere impacting at 2.5 km/s into lunar basalts. Transient crater diameter (D_{tc}) was measured at the surface level and depth (d_{tc}) was measured at the maximum excavation volume, from the surface level to the projectile residue at the bottom of the crater. x is thickness of the projectile at the end of excavation stage. Accuracy of the measurements is up to 10 cm (size of two cells in the high resolution zone). Left side of the plot shows tracer positions over density plot, and right side shows total plastic strain.

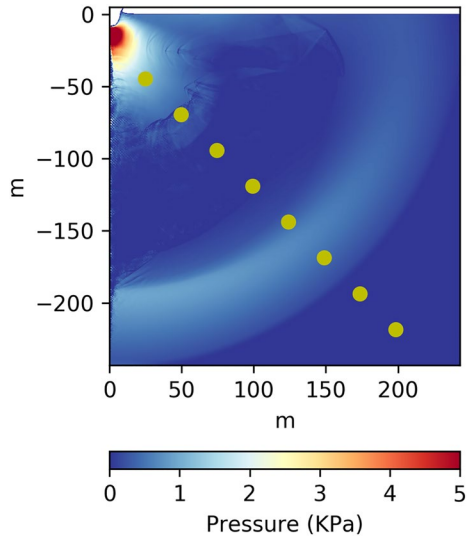

Figure 4. Position of gauges (yellow dots diagonally through the target), pre-selected cells in which data used for calculating seismic efficiency was stored. Pressure field is output from Case 2 (90% porous half cylinder) simulation.

The calculations of seismic efficiency and seismic moment required tracking the decay of the impact-induced pressure wave into the elastic regime, which occurs in the far field (here defined as radial distance ≥ 10 crater radii). As shown in previous work (Rajšić et al., 2021; Wójcicka, Collins, Bastow, Miljkovic, et al., 2020), the pressure wave can be considered elastic when pressure amplitudes become comparable with the cohesion of the target material (Table 2) (e.g., Holsapple, 1993). Therefore, the size of the computational mesh in these simulations was much larger than crater formation simulations. Depending on the projectile shape, we used 2,000 × 2,050 to 4,350 × 4,400 cells. Projectile geometry remained the same as in crater formation simulation (Table 1).

The seismic moment was estimated using the approach described by Wójcicka, Collins, Bastow, Miljkovic, et al. (2020) to determine the vertical component of the seismic moment (M_z) (Gudkova et al., 2015; Lognonné et al., 2009): $M_z = C_p \sum_i^n \rho[i]\upsilon_z[i]V[i]$, where $\rho[i]$ is the density of material in the cell, $\upsilon_z[i]$ is the cell-centered vertical velocity component, $V[i]$ is the cell volume, C_p is the P-wave velocity and the summation is over all n cells in the target (below the pre-impact level). We calculated C_p as the speed of the pressure wave between two gauges (Figure 4). For vertical impacts, this means that seismic moment is defined as $M_z = C_p p_z$, where p_z is the vertical momentum transferred to the target by the projectile (Gudkova et al., 2015; Lognonné et al., 2009; Wójcicka, Collins, Bastow, Teanby, et al., 2020), which includes both the directly transferred impactor momentum as well as the additional momentum produced by ejected material.

We also investigated into how fast momentum is transferred to the target. Since we consider strictly vertical impact scenarios, we assume that the equivalent seismic source is a vertical force (Daubar et al., 2018; Wójcicka et al., 2021), $F_z(t)$. The vertical force is computed as a derivative of the momentum transferred to the target, $p_z(t)$, with respect to time t: $Fz = dp_z(t)/dt$. Therefore, the duration of momentum transfer to the target affects the peak force at the seismic source, even if the total momentum transferred is the same.

To calculate seismic efficiency k, we used the same approach as in many previous works (e.g., Güldemeister & Wünnemann, 2017; Rajšić et al., 2021; Wójcicka, Collins, Bastow, Miljkovic, et al., 2020): $k = \pi x^2 P^2 \Delta t / (\rho C_p E_k)$, where, x is the distance from the impact point, P is the pressure amplitude, Δt is the duration of the pressure pulse measured at full width half maximum, ρ is the bulk density of the target, and E_k is the kinetic energy of the impactor. In case of the double-layered target, bulk density and P wave velocity were assumed to be as in lower layer (fractured bedrock). This is because regolith in our simulations was only 5 m thick, and calculations of seismic efficiency were performed at ~ 10 crater radii away. Data used for calculating seismic efficiency was recorded at pre-selected cells (gauges) positioned equidistant diagonally through the target (Figure 4). In our simulations, gauges imitate pressure sensors used in physical experiments. They are fixed cells in space, specified a priori and provide a straightforward way to record data used to calculate seismic efficiency since their position is known (x in the equation), and C_p is easily calculated, as a speed of pressure wave needed to come from one gauge cell to another. The duration (Δt) and amplitude (P) of the pressure pulse can also be measured at each of the gauges.

3. Results

We calculated the transient crater diameter (D_{tc}), depth (d_{tc}), and thickness of projectile residue (x) at the bottom of the transient crater (Figure 3). As our simulations do not include the modification stage of crater formation, we treat the transient crater diameter and depth as lower and upper bounds on the final crater diameter and depth, respectively. To estimate the other bound, we adopt a geometric model of simple crater formation that widens the crater by a factor of 1.25 (assuming a hemi-spherical crater) and reduces the depth by a factor of two (Collins et al., 2005). However, the observed craters are elliptical, and to account

Table 3
Results (Crater Size) From iSALE-2D Simulations (Accuracy up to 0.1 m) Compared to Observations and Scaling Laws (Melosh, 1989; Plescia et al., 2016) (d_t Is Transient Depth of the Crater; x is Projectile Residual at the End of Excavation Phase; $d_t - x$ Is Final Depth Without Projectile Residual Calculated in; D_t Is Transient Diameter; D_{fc} Is Maximum Final Crater Diameter, Multiplied by a Factor of 1.44 (1.25 for Hemispherical Crater Times 1.15 for Elongation of Observed Crater); Π_v Is Cratering Efficiency by Mass (Melosh, 1989))

Case	Description	d_{tc} (m)	x (m)	$d_{tc} - x$ (m)	d_f (m)	D_{tc} (m)	max D_{fc} (m)	Π_v
1	Right cylinder, $r = 5.8$ m	4.8	0.31	4.49	2.25	21.2	30.3	87.33
2	Right cylinder, $r = 2.8$ m	8.8	0.44	8.36	4.18	21.7	31.3	171.91
3	Thin shell, $r = 2.8$ m	9.6	0.2	9.4	4.35	23.8	34.3	179.29
4	Right cylinder, $r = 0.992$ m	13.32	3.32	10.00	5	26.7	38.4	324.28
5	Sphere, $r = 1.06$ m	9.33	0.18	9.15	4.58	25.4	36.6	264.66
6	Sphere, $r = 2.3$ m	8.26	1.76	6.5	4.3	23.41	33.7	164.29
7	Sphere, $r = 2.3$ m	7.56	1.48	6.08	3.04	24.74	35.6	171.63
	Plescia et al. (2016)				~2–6		28.6–38.7 ± 0.5	
	Melosh (1989)			8.8	4.4	26.32	32.9	271.5

for that discrepancy, from the ratio of long and short axes and the crater surface area, we applied additional ±15% correction multiplication to the final crater diameter. Table 3 shows our numerical crater measurements, the depth of transient cavity excluding the projectile residue (d_{tc}) and depth to the top of the projectile residue ($d_{tc} - x$) as well as the corrections for the final depth and diameter estimates and cratering efficiency.

Figure 5 (left; empty circles) shows the transient crater measurements from impact simulations for all cases (1–7). They include the projectile residue at the bottom of the crater. It is noticeable that crater diameter increases with a decrease in projectile footprint. The largest diameter was observed in case of vertical projection of the booster (Case 3), which has the smallest footprint. The height of the projectile and the footprint area, also affect the depth of the crater. The larger the footprint area, the smaller the depth (Figure 5). The height and footprint area had larger effect on crater size than including layer to the target (Cases 7). Differences in crater size among projectiles with same footprint but one with included porosity (Case 2) and one hollow (Case 3) are also in agreement up to a factor of 1.1. Although, on this figure, the simulated transient

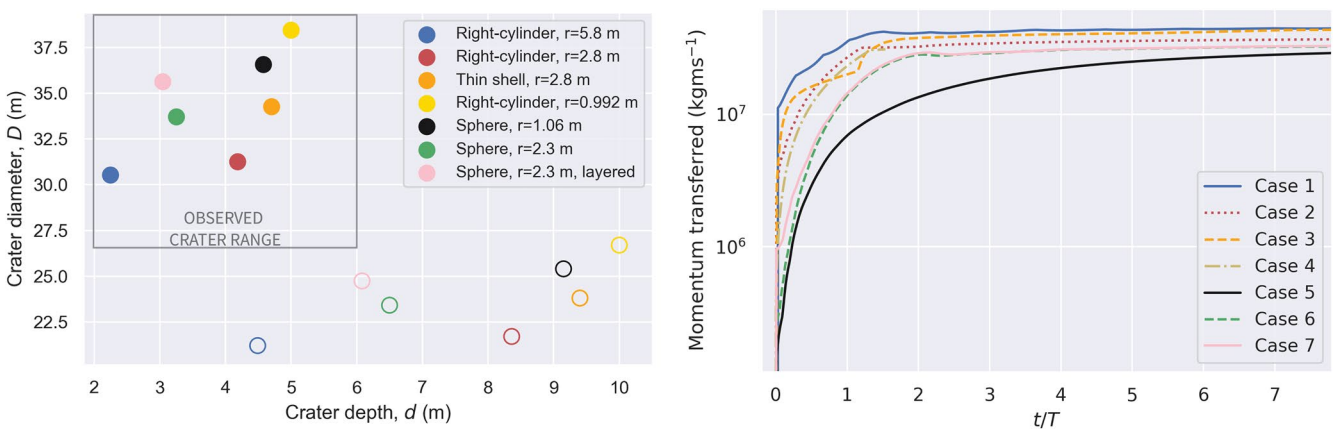

Figure 5. (left) Resulting crater depth and diameter for all cases. Empty circles show the transient crater dimensions with 2 numerical cells uncertainty (absolute values are listed in Table 2) and filled circles show the final crater dimension estimates. The crater diameter was multiplied by a factor of 1.44, to account for the simple crater growth during transient crater collapse as well as ellipticity of observed craters. The transient crater depth was divided by a factor of 2 to account for the crater collapse into the final depth. Crater depth and diameter increase with the decrease in projectile footprint area. Gray box shows measurements of depth and diameter of observed craters, with a factor of two uncertainty on the depth and the observed diameter range (from shortest to longest axis of the crater rim ellipse). (right) Impact momentum transfer to the target as a function of time normalized to the duration of the contact and compression phase (Melosh, 1989): t is time after impact and T is the duration of the contact and compression stage, where $T = L/V_i$ (L is projectile length and V_i is velocity of the impact).

craters are twice as deep and 30% wider than the observed craters, the filled circles on the same figure show estimates of final crater sizes, which are in agreement with observed crater dimensions (gray box in Figure 5). Furthermore, the depth to diameter ratio (d/D) for different projectile geometries was different. The depth to diameter ratio of the observed craters is in the range of 0.05–0.1. In our case, d/D for final crater dimension estimates in Cases 1 and 7 was 0.074 and 0.085, respectively, while all the other cases resulted in d/D ~0.13. Therefore, d/D ratio in this work is comparable to the observations and is in agreement up to a factor of 1.8 among different projectile geometries.

All projectiles in this work were made of aluminum. The critical shock pressures for incipient melting and complete melting of aluminum are $P_{im} = 73$ GPa and $P_{cm} = 106$ GPa, respectively (Pierazzo et al., 1997). The peak pressures that projectiles in this study experienced are much lower than P_{im} and P_{cm}. Although our simulations did not have sufficient spatial resolution to resolve the maximum pressures of all parts of the spacecraft, the maximum pressures experienced by the bulk of the projectiles considered in this work did not exceed 5 GPa. This is still significantly lower than what experimental studies on porous aluminum projectiles showed as required for melting (Song et al., 2011). This suggests that the projectiles predominantly remained solid at the bottom of craters.

The thickness of the projectile residue at the bottom of the crater can be estimated with an uncertainty equivalent to the length of two cell widths (see, Grid spacing in Table 1). Our simulations suggest that the longer and more porous the projectile (smaller footprint area), the thicker the residue of the projectile at the bottom of the crater. Our measurements have accuracy up to two cells. For four different cylindrical representations (Cases 1–4) of the projectile with increasing height, residual impactor thickness increases from 0.31 to 3.32 m (Table 3). Between cases 5 and 6 (non-porous and 90% porous sphere), the thickness of the residual projectile changes drastically, from 0.18 to 1.76 m (Table 3). Cases 2 and 3 had the same footprint, but the first one was porous cylinder, while the second one was thin shell. Between these cases, size of the projectile residual decreased by a factor of 2 when using thin shell representation of the booster (Case 3). This suggests that the geometry of the projectile residual at the bottom of the crater is sensitive to the geometry and density of the impacting booster as well as layering of the target. Although the aim of this study was to test projectile influence on crater size, the observed crater morphology on the Moon was most likely controlled by both the projectile's irregular shape and density as well as the presence of a stronger layer underneath the regolith.

Cratering efficiency was calculated as the ratio of the mass of displaced target material (target density multiplied by volume of the transient crater cavity) and the mass of the projectile (Melosh, 1989). Table 3 shows that the cratering efficiency varies between different projectile representations and follows the same trend as the crater diameter; the bigger the impactor footprint, the lower the cratering efficiency. The highest cratering efficiency is for Case 4, while the lowest is for Case 1. This is consistent with the increasing crater depth and diameter with the orientation of the projectile (decreasing of footprint area).

Furthermore, we investigate how the shape of the projectile affected the duration of momentum transfer to the target. While both spherical representations (Case 4 and 5) transferred momentum at about the same time after impact, in case of the cylindrical representation, the momentum transfer took from 0.3 to 8.7 ms, where the longest time is for the projectile with the smallest footprint area (Case 5) and the least time is for the largest footprint area. The latter is comparable to the real booster impacting along the longer axis (Case 1). In Figure 5 (right), we show momentum transfer to the target as a function of duration of momentum transfer normalized to the duration of the contact and compression stage. Duration of the contact and compression stage was calculated as: $T = L/V_i$ (Melosh, 1989), where L is projectile length and V_i is impact velocity. Times for complete momentum transfer varied from 0.197 ms (Case 1, right cylinder with $r = 5.8$ m) to 6.5 ms (Case 4, right cylinder with $r = 0.992$ m). When normalized to the duration of this stage, momentum transfer among projectiles that included porosity and/or void behaves similarly. The exception to this is Case 5, solid sphere, where momentum transfer takes more time to converge.

Table 4 shows the seismic efficiency, k, seismic moment M_z, and the maximum vertical force component $F_{\max}$ calculated for each scenario. Both seismic efficiency and seismic moment were calculated when the wave had passed beyond 11 crater radii (far field), when both quantities had converged (Figure 6). The mean values of Δt and P recorded by the two furthest cell gauges in the numerical mesh (Figure 6 (left)) were used

Table 4
Resulting Seismic Parameters From iSALE-2D Simulations Compared to Previous Works (Apollo 13 S-IVB From Latham et al. (1970) and Impact Momentum and Seismic Moment Scaling of Wójcicka, Collins, Bastow, Teanby, et al. (2020), See Equation 20

Case	Description	$\Delta t(ms)$	$P(Pa)$	k	$M_z(Nm)$	F_{max} (N)
1	Right cylinder, $r = 5.8$ m	45	5,243	8.27×10^{-7}	5.16×10^{10}	1.93×10^{12}
2	Right cylinder, $r = 2.8$ m	41	7,130	1.35×10^{-6}	4.50×10^{10}	4.4×10^{11}
3	Thin shell, $r = 2.8$ m	15	29,622	1.33×10^{-6}	5.3×10^{10}	5.56×10^{11}
4	Right cylinder, $r = 0.992$ m	32	8,498	1.20×10^{-6}	3.88×10^{10}	5.8×10^{10}
5	Sphere, $r = 1.06$ m	37	5,024	1.43×10^{-6}	4.3×10^{10}	2.3×10^{10}
6	Sphere, $r = 2.3$ m	40	4,741	1.04×10^{-6}	3.95×10^{10}	4.2×10^{10}
7	Sphere, $r = 2.3$ m (layered target)	6	14,302	1.97×10^{-6}	7.35×10^{10}	5.56×10^{11}
	Latham et al. (1970)			$10^{-6} - 10^{-5}$		
	Wójcicka, Collins, Bastow, Miljkovic, et al. (2020)			10^{-6}	$5.3–10.9 \times 10^{10}$	

Note. Δt is duration of the pressure pulse; P is pressure amplitude; k is seismic efficiency; M_z is vertical seismic moment component; and F_{max} peak force at the seismic source.

for calculating k. The seismic moment values presented in Table 4 are mean values of the three last measurements of seismic moment taken from the simulation (Figure 6 (right)).

Despite the significant differences in crater size, geometry, and momentum transfer duration, the seismic moment and efficiency of all seven scenarios are very similar. Seismic efficiency ranges from 8.3 to 1.4×10^{-6}, which is consistent with the lower-bound estimate of k determined from the Apollo seismic measurements (Latham et al., 1970). This narrow range of seismic efficiency is also consistent with values of seismic efficiency determined from iSALE simulations of small rocky impactors striking Mars at a few kms^{-1} that employed the same target model as used here (Wójcicka, Collins, Bastow, Miljkovic, et al., 2020). Cases 6 and 7, are both same porous sphere projectiles, impacting two different targets, pure regolith and a layered target, and between them seismic efficiency has increased ~2 times. This suggests that while seismic efficiency does depend on target properties (Rajšić et al., 2021), it is relatively insensitive to impactor properties, such as geometry and density. Although, seismic efficiency between porous cylindrical projectiles (Cases 1 and 2) and projectile that included void (Case 3) was similar, in Table 4 we also show the duration of the isolated pressure pulse and its amplitude. In Case 3, pressure amplitude was significantly higher and duration of the pressure pulse significantly lower than in porous cases. This suggests that while

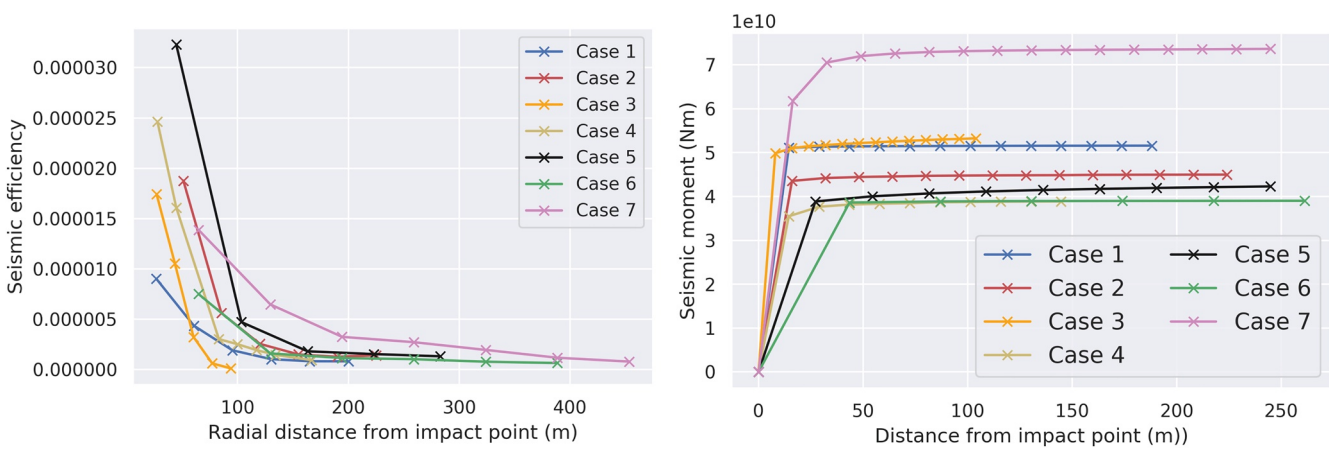

Figure 6. (left) Convergence of the seismic efficiency with distance from the impact point. (right) Convergence of the seismic moment with distance from the impact point. Seismic moment needed less time to converge than seismic efficiency. In both cases, the points correspond to the measurements from iSALE simulations. Cases are 1–5 shown in blue, red, yellow, black, and green, respectively.

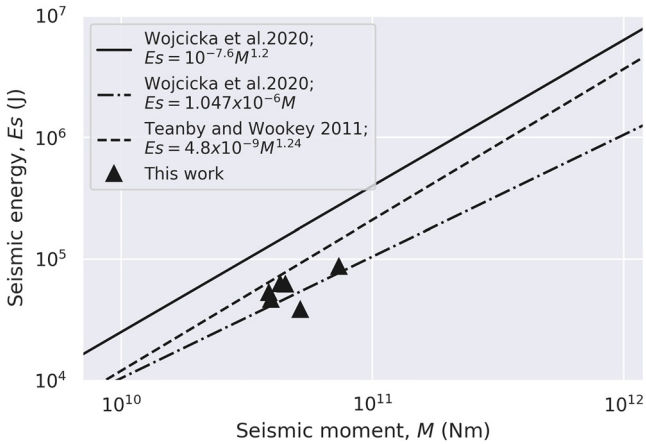

Figure 7. Scaling relationships between seismic moment (M) and seismic energy (E_s) from different studies are shown in different line styles. Our simulations were made for a regolith target and layered target (triangles), which best agrees with the scaling relationships of Wójcicka, Collins, Bastow, Teanby, et al. (2020) shown in dash-dotted line.

seismic efficiency, seismic moment, and crater size might be insensitive to the spacecraft representation, the frequency content of the generated seismic waves may differ.

The impact momentum transferred to the target is the same in all cases, but the peak applied force varies by two orders of magnitude among cases (Table 4). This is due to the difference in time it takes to transfer momentum from the impactor to the target caused by different projectile representations (Figure 5 (right)). The seismic source duration can be related to the impact momentum Gudkova et al. (2011, 2015). The real time of our simulations was 10 ms (limited by computational resources); therefore, estimating the seismic source duration was not achieved. However, by 10 ms, the force amplitude drops three orders of magnitude in Cases 1 and 2 and one order magnitude for Cases 3–5. Furthermore, in this short time frame, the force amplitude for all cases converges to the same value (3.85×10^9 N) (Figure S2 in Supporting Information S1).

4. Discussion

Our results show that the irregular shape and hollow structure of the S-IVB boosters affected crater size in these artificial impacts on the Moon (Figure 1). Craters made by S-IVB boosters show central mounds at the bottom of the crater. In craters this size formed by natural hypervelocity impacts with solid impactors, central mounds typically imply the presence of a stronger layer beneath the surface (e.g., Prieur et al., 2018; Quaide & Oberbeck, 1968). Plescia et al. (2016) argued that the central mounds in the S-IVB craters were likely a result of the low-density impactor as opposed to target property effects. Our results demonstrate that differences in the density and geometry of the projectile resulted in different thicknesses of projectile remnants in the bottom of the crater. The geometry and bulk porosity of the projectile had an effect on the size of the crater, including both depth and diameter of the crater and thickness of projectile residual. The larger the footprint area of the impactor, the shallower and smaller in diameter the crater. On the other hand, between cylinder with added porosity (Case 2) and the hollow cylinder (Case 3), but same footprint and mass, both diameter and depth of the transient crater are in agreement up to a factor of 1.1. However, adding 90% porosity in Case 2 resulted in two times larger projectile residual at the bottom of the crater. This implies that on the size of the crater, length and height of projectile had a bigger effect than its porosity. On the other hand, thickness of projectile residual showed sensitivity to both. Therefore, if no melting and vapourization occurs during this phase, for the same densities, the taller the projectile the more of it remains after at the bottom of the crater. The same changes also increased the cratering efficiency and the time required to transfer impact momentum to the target. We calculate the peak force of the seismic source as the vertical momentum transferred to the target over time showing that the faster the momentum transferred to the target, the higher the peak force.

Our results demonstrate that seismic moment and seismic efficiency are largely independent of the geometry and bulk porosity of the projectile. Regardless of whether the spacecraft is represented as a hollow structure or a homogeneous porous cylinder or sphere of the same mass, the seismic efficiency estimated from our numerical impact simulations is in agreement up to a factor of a 1.7 for all projectile representations and increases up to 2 times in a layered target. The average estimate agrees with the lower estimates of Latham et al. (1970) that derived the seismic efficiency of the Moon from impact-induced moonquake observations. This suggests that seismic efficiency is more sensitive to target properties, as shown in previous work (Rajšić et al., 2020), than to impactor properties. Similarly, the seismic moment is within a factor of only 1.3 for all cases of regolith targets. In addition to seismic efficiency, seismic moment in layered target increases up to 2 times. These values, both in regolith and layered target, are in agreement with scaling relationships between seismic moment and seismic energy (Teanby, 2015; Wójcicka, Collins, Bastow, Teanby, et al., 2020) (Figure 7).

The seismic moment calculated from our simulation results is for a homogeneous regolith target. As discussed by Daubar et al. (2018), the appropriate seismic moment to use as a source magnitude for predicting

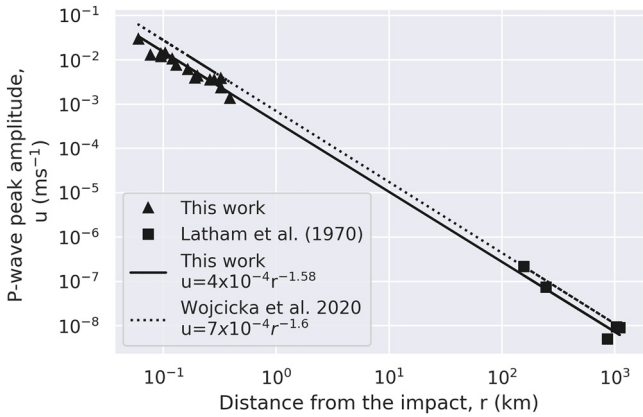

Figure 8. P wave amplitude scaled with distance and compared to recent scaling relationship (Fernando et al., 2020). We found that best trend fit between our data (triangles) and lunar observations (squares; Latham et al. [1970]) is $v = 4 \times 10^{-4} r^{-1.58}$, where r is the radial distance from the impact point in km. Data from this work was calculated between 100 and 400 m distance from the impact point for all cases and showed more than 10 data points cumulatively across all cases investigated in this study.

far field seismic wave signals that propagate through bedrock and neglect the surface regolith layer should include a correction to account for the difference in material properties between the regolith and bedrock. To estimate the magnitude of the seismic moment for use in seismic modeling, we calculated the bedrock correction factor, T_m, composed of two elements as described in (Daubar et al., 2018). Here, those two factors combined equate to $T_m = 2\rho_{br}\upsilon_{br}^3/(\upsilon^2(\rho_{br}\upsilon_{br} + \rho\upsilon))$, where ρ and ρ_{br} are densities of the regolith and bedrock (1,500 kg·m^{-3} and 2,700 kg·m^{-3}, respectively), and υ and υ_{br} are P-wave velocities in regolith and bedrock (300 ms^{-1} and 1,000 ms^{-1}, respectively). In this case, to replicate far field effects of the S-IVB impacts in wave propagation models without explicitly resolving the effects of the near-surface regolith, a scalar seismic moment should be increased by as much as 20 times.

The peak P-wave amplitudes of the seismic signals generated by the S-IVB artificial impacts and recorded by Apollo seismometers 100–1,000 km from the impact sites (Latham et al., 1970) form the basis of empirical amplitude-distance scaling relationships for predicting the seismic detectability of impacts (Teanby, 2015; Wójcicka, Collins, Bastow, Teanby, et al., 2020). Our numerical simulations allow these scaling relationships to be tested against, and refined by, P-wave amplitude estimates at distances much closer to the impact location (Figure 8). For all five impact scenarios, we calculated the peak P-wave amplitude (in meters per second) as the time-derivative of the radial displacement of material at distances from the impact between 100 and 400 m (triangles, Figure 8). The simulated peak P-wave amplitudes are about a factor of two less than predicted by the empirical scaling relationships of Teanby (2015) and Wójcicka, Collins, Bastow, Teanby, et al. (2020). Taking these new synthetic data into account, the empirical scaling relationship between peak P-wave amplitude, distance, and crater size, from Wójcicka, Collins, Bastow, Teanby, et al. (2020) can be updated to $v(x, D) = 8.11 \times 10^{-9} \xi_2 x^{-1.58} D^3$, where, v is P-wave peak amplitude (m s^{-1}), D is crater diameter, and ξ_2 is a factor that depends on impactor and target properties (for details see: Equation 21; Wójcicka, Collins, Bastow, Teanby, et al. [2020]). This revised relationship results in 20% lower P-wave peak amplitudes produced by a given crater size than previously predicted.

5. Conclusions

This work connected numerical impact simulations with seismic parameters related to the Apollo S-IVB artificial impacts on the Moon that were recorded by the lunar seismic network. Compared to previous work, the focus of this study was the geometric representation of the impactor and resulting crater formation. After confirming that our simulations are approximately consistent with observed crater dimensions, further simulations were performed to investigate the generation of the seismic source and calculate seismic properties associated with the impact event (the seismic efficiency and the seismic moment). This work contributes to the understanding of the seismicity induced by impact cratering events as well as detectability of impacts in seismic data, and there are several outcomes of this study:

1. We have replicated the artificial impacts of the S-IVB boosters on the Moon with a simplified projectile geometry and investigated the sensitivity of crater size and shape, as well as the seismic waves that are generated, to impactor density and geometry (e.g., footprint area on the ground).
2. A final crater with dimensions consistent with the observed craters can be produced by a range of impactor geometries, but the detailed morphology is sensitive to the geometry and bulk density of the impactor. To replicate the detailed morphometry would likely require 3D simulations that account for oblique impact and more realistic S-IVB booster geometries.
3. Among three different projectile representations with similar footprint area: porous sphere, porous right cylinder, and hollow cylinder, the resulting crater geometry and momentum transfer did not show significant differences.

4. Scenarios with a realistic low bulk density for the impactor produce a substantial projectile residual. This suggests that the observed central mound in S-IVB craters may represent surviving spacecraft material, which may or may not be buried by collapsed crater rim materials. We have also tested a scenario with a stronger layer underneath the 5 m thick regolith. Our simulations indicate that the irregular shapes of the artificial craters on the Moon could be a result of both the properties of the booster and the layering in the target.
5. The seismic efficiency and seismic moment of the impact is almost independent of impactor geometry. A seismic efficiency of 10^{-6} is consistent with lower estimates of Latham et al. (1970). Seismic moment calculated from our simulations is in order of 4×10^{10} Nm, which is in agreement with scaling of (Teanby, 2015; Wójcicka, Collins, Bastow, Teanby, et al., 2020).
6. Seismic efficiency and seismic moment in the layered target, where 5 m of regolith overlies fractured bedrock, increase by a factor of 2. This implies that seismic parameters depend more on target properties than projectile representation.
7. We compared P-wave peak amplitudes from our simulations to the ones observed on Apollo seismometers (Latham et al., 1970) and found that P-wave peak amplitudes decay with radial distance from impact point with an exponent of ~ -1.58, which is consistent with scaling relationships derived in Wójcicka, Collins, Bastow, Teanby, et al. (2020).

Data Availability Statement

Input files and data used in this work are located at Rajšić (2021). This work is InSight contribution number 201.

Acknowledgments
A. Rajšić and K. Miljković are fully funded by the Australian Government through the ARC (DE180100584, DP180100661). N. Wójcicka and G. S. Collins research is funded by the UK Space Agency (Grants ST/S001514/1 and ST/T002026/1). I. J. Daubar was supported by NASA InSight Participating Scientist grant 80NSSC20K0971. The authors gratefully acknowledge the developers of iSALE (https://isale-code.github.io).

References

Amsden, A., Ruppel, H., & Hirt, C. (1980). *Sale: A simplified ale computer program for fluid flow at all speeds* (Technical Report). Los Alamos Scientific Laboratory.

Banerdt, W. B., Smrekar, S. E., Banfield, D., Giardini, D., Golombek, M., Johnson, C. L., et al. (2020). Initial results from the InSight mission on Mars. *Nature Geoscience*, *13*(3), 183–189.

Collins, G. S., Melosh, H. J., & Ivanov, B. A. (2004). Modeling damage and deformation in impact simulations. *Meteoritics & Planetary Science*, *39*(2), 217–231. https://doi.org/10.1111/j.1945-5100.2004.tb00337.x

Collins, G. S., Melosh, H. J., & Marcus, R. A. (2005). Earth impact effects program: A web-based computer program for calculating the regional environmental consequences of a meteoroid impact on Earth. *Meteoritics & Planetary Science*, *40*(6), 817–840. https://doi.org/10.1111/j.1945-5100.2005.tb00157.x

Colwell, J., Batiste, S., Horányi, M., Robertson, S., & Sture, S. (2007). Lunar surface: Dust dynamics and regolith mechanics. *Reviews of Geophysics*, *45*(2). https://doi.org/10.1029/2005rg000184

Daubar, I., Lognonné, P., Teanby, N., Collins, G., Clinton, J., Stähler, S., et al. (2020). A new crater near insight: Implications for seismic impact detectability on mars. *Journal of Geophysical Research: Planets*, *125*(8), e2020JE006382. https://doi.org/10.1029/2020je006382

Daubar, I., Lognonné, P., Teanby, N. A., Miljkovic, K., Stevanović, J., Vaubaillon, J., et al. (2018). Impact-seismic investigations of the InSight mission. *Space Science Reviews*, *214*(8), 1–68. https://doi.org/10.1007/s11214-018-0562-x

Fernando, B., Wojcicka, N., Froment, M., Maguire, R., Staehler, S., Rolland, L., et al. (2020). *Listening for the landing: Detecting perseverance's landing with InSight*.

Gudkova, T., Lognonné, P., & Gagnepain-Beyneix, J. (2011). Large impacts detected by the Apollo seismometers: Impactor mass and source cutoff frequency estimations. *Icarus*, *211*(2), 1049–1065. https://doi.org/10.1016/j.icarus.2010.10.028

Gudkova, T., Lognonné, P., Miljković, K., & Gagnepain-Beyneix, J. (2015). Impact cutoff frequency–momentum scaling law inverted from Apollo seismic data. *Earth and Planetary Science Letters*, *427*, 57–65. https://doi.org/10.1016/j.epsl.2015.06.037

Güldemeister, N., & Wünnemann, K. (2017). Quantitative analysis of impact-induced seismic signals by numerical modeling. *Icarus*, *296*, 15–27. https://doi.org/10.1016/j.icarus.2017.05.010

Holsapple, K. A. (1993). The scaling of impact processes in planetary sciences. *Annual Review of Earth and Planetary Sciences*, *21*(1), 333–373. https://doi.org/10.1146/annurev.ea.21.050193.002001

Johnson, G. R., & Cook, W. H. (1983). A constitutive model and data for metals subjected to large strains, high strain rates and high temperatures. In *Proceedings of the 7th international symposium on ballistics* (Vol. 21, pp. 541–547).

Latham, G., Ewing, M., Dorman, J., Press, F., Toksoz, N., Sutton, G., et al. (1970). Seismic data from man-made impacts on the Moon. *Science*, *170*(3958), 620–626. https://doi.org/10.1126/science.170.3958.620

Liu, Q., Fu, J., Wang, J., Ma, J., Chen, H., Li, Q., & Hui, D. (2017). Axial and lateral crushing responses of aluminum honeycombs filled with EPP foam. *Composites Part B: Engineering*, *130*, 236–247. https://doi.org/10.1016/j.compositesb.2017.07.041

Lognonné, P. (2005). Planetary seismology. *Annual Review of Earth and Planetary Sciences*, *33*, 571–604. https://doi.org/10.1146/annurev.earth.33.092203.122604

Lognonné, P., Le Feuvre, M., Johnson, C. L., & Weber, R. C. (2009). Moon meteoritic seismic hum: Steady state prediction. *Journal of Geophysical Research: Planets*, *114*(E12). https://doi.org/10.1029/2008je003294

Lognonné, P., & Mosser, B. (1993). Planetary seismology. *Surveys in Geophysics*, *14*(3), 239–302.

Lundborg, N. (1968). Strength of rock-like materials. In *International Journal of Rock Mechanics and Mining Sciences & Geomechanics Abstracts* (Vol. 5, pp. 427–454). https://doi.org/10.1016/0148-9062(68)90046-6

Mc Fadden, W., & Salzberg, I. (1970). *AS-508 S-4B postflight lunar impact trajectory analysis* (NASA TM X-64563). NASA Technical Memorandum.
McGarr, A., Latham, G. V., & Gault, D. E. (1969). Meteoroid impacts as sources of seismicity on the moon. *Journal of Geophysical Research*, *74*(25), 5981–5994. https://doi.org/10.1029/jb074i025p05981
McKay, D. S., Heiken, G., Basu, A., Blanford, G., Simon, S., Reedy, R., et al. (1991). The lunar regolith. In *Lunar sourcebook* (Vol. 7, pp. 285–356). Citeseer.
Melosh, H. J. (1989). *Impact cratering: A geologic process*. ICGP.
Mitchell, J., Houston, W., Carrier, W., III, & Costes, N. (1974). *Apollo soil mechanics experiment S-200*.
Onodera, K., Kawamura, T., Tanaka, S., Ishihara, Y., & Maeda, T. (2021). Numerical simulation of lunar seismic wave propagation: Investigation of subsurface scattering properties near Apollo 12 landing site. *Journal of Geophysical Research: Planets*, *126*(3), e2020JE006406. https://doi.org/10.1029/2020je006406
Pierazzo, E., Vickery, A., & Melosh, H. (1997). A reevaluation of impact melt production. *Icarus*, *127*(2), 408–423. https://doi.org/10.1006/icar.1997.5713
Plescia, J., Robinson, M., Wagner, R., & Baldridge, R. (2016). Ranger and Apollo S-IVB spacecraft impact craters. *Planetary and Space Science*, *124*, 15–35. https://doi.org/10.1016/j.pss.2016.01.002
Prieur, N. C., Rolf, T., Wünnemann, K., & Werner, S. C. (2018). Formation of simple impact craters in layered targets: Implications for lunar crater morphology and regolith thickness. *Journal of Geophysical Research: Planets*, *123*(6), 1555–1578. https://doi.org/10.1029/2017je005463
Quaide, W. L., & Oberbeck, V. R. (1968). Thickness determinations of the lunar surface layer from lunar impact craters. *Journal of Geophysical Research*, *73*(16), 5247–5270. https://doi.org/10.1029/jb073i016p05247
Rajšić, A. (2021). *Numerical simulations of Apollo S-IVB artificial impacts on the Moon*. https://doi.org/10.5281/zenodo.5715855
Rajšić, A., Miljković, K., Collins, G., Wünnemann, K., Daubar, I., Wójcicka, N., & Wieczorek, M. (2021). Seismic efficiency for simple crater formation in the Martian top crust analogue. *Journal of Geophysical Research: Planets*, *126*(2), e2020JE006662.
Rajšić, A., Miljković, K., Collins, G., Wünnemann, K., Wieczorek, M., Wójcicka, N., & Daubar, I. (2020). Effects of target properties on seismic efficiency in meter-size craters on Mars. In *Lunar and Planetary Science Conference* (Vol. 2326, p. 1793).
Song, P., Cai, L.-C., Wang, Q.-S., Zhou, X.-M., Li, X., Zhang, Y., et al. (2011). Sound velocity, temperature, melting along the Hugoniot and equation of state for two porosity aluminums. *Journal of Applied Physics*, *110*(10), 103522. https://doi.org/10.1063/1.3662193
Teanby, N. (2015). Predicted detection rates of regional-scale meteorite impacts on Mars with the InSight short-period seismometer. *Icarus*, *256*, 49–62. https://doi.org/10.1016/j.icarus.2015.04.012
Tillotson, J. H. (1962). *Metallic equations of state for hypervelocity impact* (Technical Report). General dynamics San Diego CA General Atomic Division.
Toksöz, M. N., Dainty, A. M., Solomon, S. C., & Anderson, K. R. (1974). Structure of the Moon. *Reviews of Geophysics*, *12*(4), 539–567. https://doi.org/10.1029/rg012i004p00539
Wagner, R., Nelson, D., Plescia, J., Robinson, M., Speyerer, E., & Mazarico, E. (2017). Coordinates of anthropogenic features on the Moon. *Icarus*, *283*, 92–103. https://doi.org/10.1016/j.icarus.2016.05.011
Walker, J. D. (1999). A model for penetration by very low aspect ratio projectiles. *International Journal of Impact Engineering*, *23*(1), 957–966. https://doi.org/10.1016/s0734-743x(99)00138-4
Wilcox, B., Robinson, M., Thomas, P., & Hawke, B. (2005). Constraints on the depth and variability of the lunar regolith. *Meteoritics & Planetary Science*, *40*(5), 695–710. https://doi.org/10.1111/j.1945-5100.2005.tb00974.x
Wójcicka, N., Collins, G., Bastow, I., Miljkovic, K., & Rajsic, A. (2021). Seismic source time function and frequency content of impact-generated seismic waves. In *Lunar and Planetary Science Conference* (p. 2134).
Wójcicka, N., Collins, G., Bastow, I., Miljkovic, K., Rajsic, A., Teanby, N., & Team, I. (2020). Seismic moment of small impacts on Mars. In *Lunar and Planetary Science Conference* (Vol. 2326, p. 2143).
Wójcicka, N., Collins, G. S., Bastow, I. D., Teanby, N. A., Miljković, K., Rajšić, A., et al. (2020). The seismic moment and seismic efficiency of small impacts on Mars. *Journal of Geophysical Research: Planets*, *125*(10), e2020JE006540. https://doi.org/10.1029/2020je006540
Wünnemann, K., Collins, G., & Melosh, H. (2006). A strain-based porosity model for use in hydrocode simulations of impacts and implications for transient crater growth in porous targets. *Icarus*, *180*(2), 514–527. https://doi.org/10.1016/j.icarus.2005.10.013
Wünnemann, K., Nowka, D., Collins, G., Elbeshausen, D., & Bierhaus, M. (2011). Scaling of impact crater formation on planetary surfaces—Insights from numerical modeling. In *Proceedings of the 11th hypervelocity impact symposium* (Vol. 120, pp. 1–16).